

S. A. Coronel, J. Melguizo-Gavilanes, S. Jones and J. E. Shepherd.  
Temperature field measurements of thermal boundary layer and wake of  
moving hot spheres using interferometry.  
Experimental Fluid and Thermal Science, 90:76-83, 2018.  
Available at <http://dx.doi.org/10.1016/j.expthermflusci.2017.08.031>.

## Supplementary Material

### Appendix A. Uncertainty Analysis

This Appendix provides a step by step procedure for quantifying the error in the processed temperature (interferogram→wrapped optical phase→phase unwrapping→bias removal→inversion of the Abel transform→processed temperature) due to the phase demodulation, algorithm used for the inversion of the Abel transform, and the straight ray path assumption.

The error introduced through the image processing is investigated by creating synthetic interferograms with added noise that represented the noise observed in the experimental interferograms. The synthetic interferograms are generated from synthetic temperature distributions that simulate typical temperature profiles found experimentally. First, the optical phase difference is calculated by performing ray tracing of refracted rays traveling through the disturbed medium and their corresponding interfering rays traveling through an undisturbed medium. Once the optical phase difference is obtained, a synthetic interferogram is generated and noise is added to simulate typical noise found in the experimental interferograms. Afterwards, the image post-processing is performed on the noisy synthetic interferogram to calculate the processed temperature and the error,  $\varepsilon_T$ , between the processed temperature and synthetic temperature. The error corresponds to the cumulative error of the phase demodulation, inversion algorithm, and straight ray path assumption. The procedure developed to determine the uncertainty due to the image post-processing is listed below:

1. Create synthetic temperature,  $T$ , field

2. Compute the density,  $\rho$ , using the ideal gas law
3. Compute the refractive index,  $n$ , using the Gladstone-Dale relation
4. Perform ray tracing of refracted rays through disturbed medium and reference rays through undisturbed medium to calculate the optical phase difference
5. Add bias to optical phase difference
6. Wrap biased optical phase difference between  $-\pi$  and  $\pi$
7. Extract the phase from the wrapped optical phase difference to create synthetic interferogram
8. Add noise to synthetic interferogram
9. Perform image post-processing procedure detailed in paper to calculate processed temperature
10. Compare processed temperature with synthetic temperature to calculate the error

A schematic of a refracted ray traveling through a disturbed axisymmetric medium and its corresponding reference ray (ray that travels through undisturbed medium with refractive index  $n_0$ ) is shown in Fig. A.1. Path ABC corresponds to the path taken by the refracted ray as it passes through the disturbed medium and path DEF corresponds to the path taken by the reference ray as it passes through an undisturbed medium. The two rays shown interfere and have the same optical phase at points A and D; beyond C and F, both rays will traverse the same optical path length if a lens is used to form an image of the center plane of the phase object. Vest [1] determined that the interference patterns are due to the difference in optical phase of the refracted ray as it travels through ABC and the reference ray as it travels

through DEF. Therefore, the optical phase difference between the refracted ray and reference ray is,

$$\Delta\varphi = \frac{2\pi}{\lambda} \int_A^B n(s) ds + n_0(\overline{BC} - \overline{DEF}), \quad (\text{A.1})$$

where  $s$  is the path of the refracted ray.

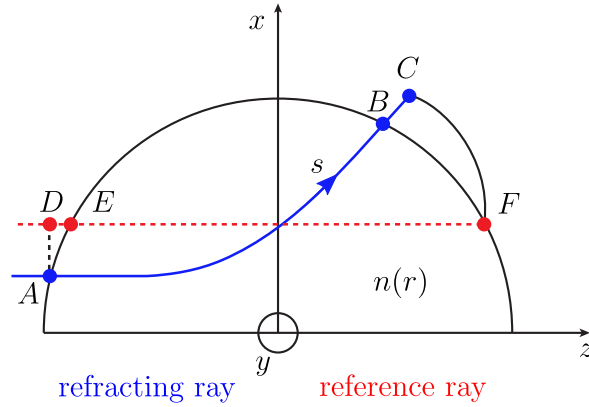


Figure A.1: Strongly refracted ray (blue) passing through disturbed medium and reference ray (red) passing through undisturbed medium, schematic adapted from Vest [1].

The path of the refracted ray through the disturbed medium and corresponding refractive index profile is calculated by using Snell's law.

$$\frac{\sin \alpha_{i-1}}{\sin \alpha_i} = \frac{n_i}{n_{i-1}} \quad (\text{A.2})$$

In Eq. A.2,  $\alpha_i$  is the incident angle on the interface between the medium at  $i-1$  and the medium at  $i$ . The index  $i$  corresponds to different points along  $s$ . The corresponding reference ray is located at a vertical distance  $\overline{AD}$  from the initial entrance location,  $A$ , of the refracted ray.  $\overline{AD}$  is the vertical distance from point  $A$  to where the straight line drawn from path  $BC$  intersects the  $x$ -axis. The reference ray at that location is the interfering ray since the

plane at  $z = 0$  is being focused by a lens onto an image plane, similar to the experimental interferometer setup described in the paper.

To start the ray tracing, axisymmetric temperature fields are generated on the  $x - z$  plane. The temperature field tested simulates the temperature field in the thermal boundary layer of the hot sphere near the region of flow separation. The top half of the temperature field is shown in Fig. A.2. The maximum temperature,  $T_{\max}$ , is 1400 K and the freestream temperature,  $T_{\infty}$ , is 300 K. The density field is computed from the temperature field by using the ideal gas law and then the refractive index is calculated by using the Gladstone-Dale relation.

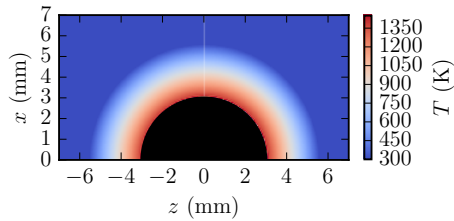


Figure A.2: Temperature field simulating the temperature profile in thermal boundary layer of the hot sphere near the region of flow separation.

The synthetic refractive index field is used as an input in the ray tracing algorithm described in Table A.1. The variables defined in the algorithm are illustrated in the images of filled contours of refractive index shown in Figs. A.3, A.4, and A.5. Figure A.3 shows the ray at an incoming angle  $\alpha_4$  measured relative to the normal axis of contour  $n_4$ . The outgoing angle,  $\beta_4$ , of the ray is measured relative to normal axis of contour  $n_4$ .  $\theta_4$  is the angle

of the outgoing ray measured relative to the axis parallel to the  $z$ -axis.

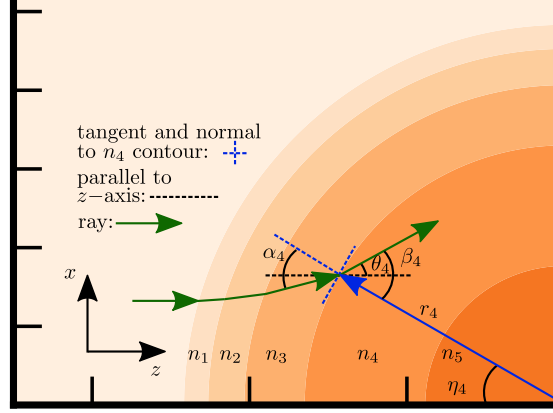


Figure A.3: Illustration of ray tracing angles in axisymmetric medium; filled contours of refractive index.

Figure A.4 illustrates the method used to determine if the ray originating at  $(z_3, x_3)$  travels to the next concentric circle,  $n_4$ , or if it remains on the same concentric circle,  $n_3$ . These two options are illustrated in Fig. A.5. The value  $x_h$ , shown in Fig. A.4, is the location where the ray originating at  $(z_3, x_3)$  would intersect the  $x$ -axis if traveling in a straight path. Figure A.5 shows that if  $x_h > r_4$ , the ray travels to the same concentric circle of  $n_3$  and if  $x_h \leq r_4$ , the ray travels to the next concentric circle  $n_4$ .

The algorithm shown in Table A.1 is applied to different values of  $x_1$  corresponding to the distance of the refracted ray from the  $z$ -axis. This is illustrated in Fig. A.1 as the  $x$ -coordinate of point A. Equation A.1 is applied to each ray to determine the optical phase difference.

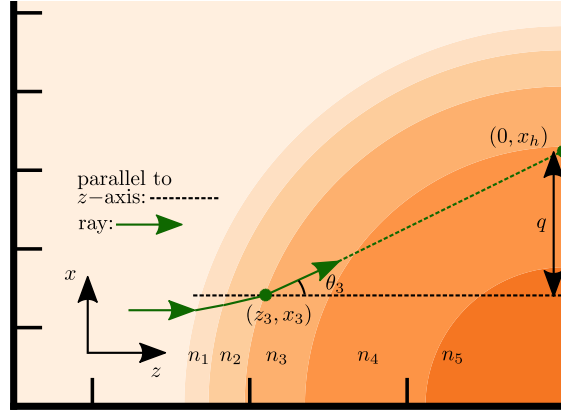


Figure A.4: Illustration of ray tracing parameter  $x_h$  in axisymmetric medium; filled contours of refractive index.

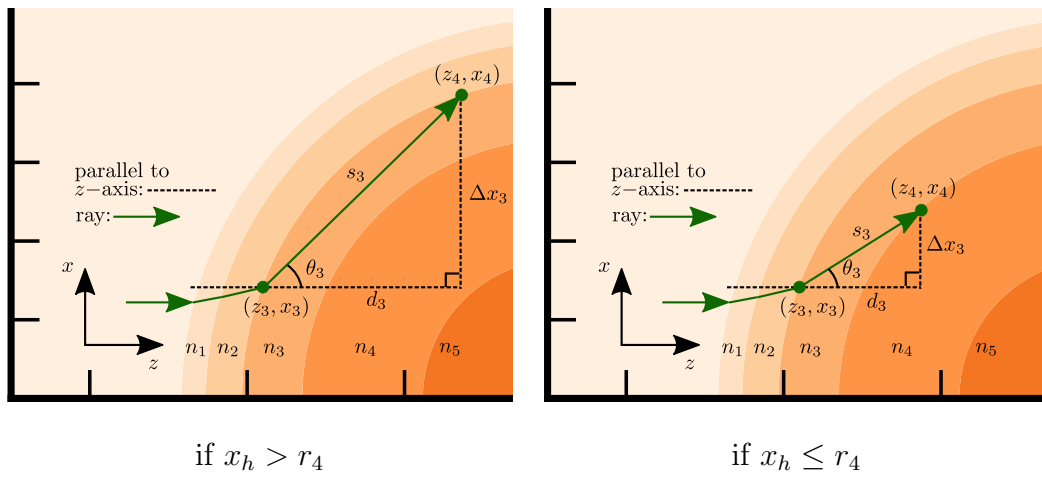


Figure A.5: Illustration of ray tracing parameters  $s_i$ ,  $\Delta x_i$ ,  $d_i$  (where  $i = 3$ ) in axisymmetric medium; filled contours of refractive index.

Table A.1: Algorithm for ray tracing through axisymmetric medium.

---

1:	<b>Inputs:</b> $x_1, \Delta r, n$
2:	<b>Outputs:</b> $x, y, s$
3:	$\theta_0 = 0, i = 0, R = r_N$
4:	<b>while</b> $z_i \leq r_N$
5:	$i = i + 1$
5:	$\eta_i = \sin^{-1} \left( \frac{x_i}{R} \right)$
6:	<b>if</b> $z_i < 0$
7:	$\alpha_i = \eta_i + \theta_{i-1}$
8:	$\beta_i = \sin^{-1} \left( \frac{n(R + \Delta r) \sin \alpha_i}{n(R)} \right)$
12:	$\theta_i = \beta_i + \eta_i$
8:	<b>else</b>
9:	$\alpha_i = \eta_i - \theta_{i-1}$
10:	$\beta_i = \sin^{-1} \left( \frac{n(R - \Delta r) \sin \alpha_i}{n(R)} \right)$
14:	$\theta_i = -\beta_i + \eta_i$
15:	<b>if</b> $i = 1$
16:	$z_i = R \cos \eta_i$
17:	<b>if</b> $z_i < 0$
17:	$q = z_i \tan \theta_i$
18:	$x_h = q + x_i$
19:	<b>if</b> $x_h > R - \Delta r$
20:	$x_{i+1}, z_{i+1} \leftarrow z_{i+1}^2 + x_{i+1}^2 = R^2$ and $x_{i+1} = (z_{i+1} + z_i) \tan \theta_i - x_i$
21:	$R = R$
21:	<b>else</b>
22:	$x_{i+1}, z_{i+1} \leftarrow z_{i+1}^2 + x_{i+1}^2 = (R - \Delta r)^2$ and $x_{i+1} = (z_{i+1} + z_i) \tan \theta_i - x_i$
23:	$R = R - \Delta R$
24:	<b>else</b>
22:	$x_{i+1}, z_{i+1} \leftarrow z_{i+1}^2 + x_{i+1}^2 = (R + \Delta r)^2$ and $x_{i+1} = (z_{i+1} + z_i) \tan \theta_i - x_i$
23:	$R = R + \Delta R$
23:	$d_i = z_{i+1} - z_i$
24:	$\Delta x_i = x_{i+1} - x_i$
25:	$s_i = \sqrt{d_i^2 + \Delta x_i^2}$

---

The algorithm of Table A.1 is validated using a refractive index equation with known optical phase difference solution presented by Kahl and Mylin [2]. The example used for validation is the case of an axisymmetric disturbance that generates constant refractive field,  $n_1$ . The refractive field is given by

$$n_0 \cos \gamma = n_1 \cos \left( \gamma + \frac{\psi}{2} \right), \quad (\text{A.3})$$

and the solution for the optical phase difference is,

$$\Delta\varphi = \frac{2\pi}{\lambda} R n_0 \left( 2 \frac{n_1}{n_0} \sin \left( \gamma + \frac{\psi}{2} \right) - 2 \sin \gamma - \cos \gamma \tan \gamma \right) \quad (\text{A.4})$$

An average error of  $2 \times 10^{-4}\%$  is found between the solution of Eq. A.4 and the numerical solution obtained with the ray tracing algorithm of Table A.1.

With the algorithm validated, the profile of optical phase difference is expanded onto two dimensions to visualize and simulate the 2D interferograms that are generated experimentally. It should be noted that the 2D synthetic optical phase difference field does not simulate the gradients in the  $y$ -direction observed around the hot sphere. Performing ray tracing along one  $z - x$  plane is already computationally expensive, therefore, performing ray tracing along all the planes shown in the experimental images requires additional computational resources or optimization of the algorithm. A bias of 200 rad is added to the optical phase difference field and subsequently wrapped from  $-\pi$  to  $\pi$ . The bias is added so the fringes in the synthetic wrapped field,  $\Delta\varphi_W$ , match up with the number of horizontal fringes present in the experimental interferograms. The phase, shown in Fig. A.6 (a), is extracted from the synthetic wrapped optical phase difference field using

$$I = \cos \Delta\varphi_W. \quad (\text{A.5})$$

Finally, random noise of 10% is added to the phase to generate the synthetic interferogram shown in Fig. A.6 (b). The image post-processing is applied to the interferogram of Fig. A.6 (b) to obtain a processed temperature field.

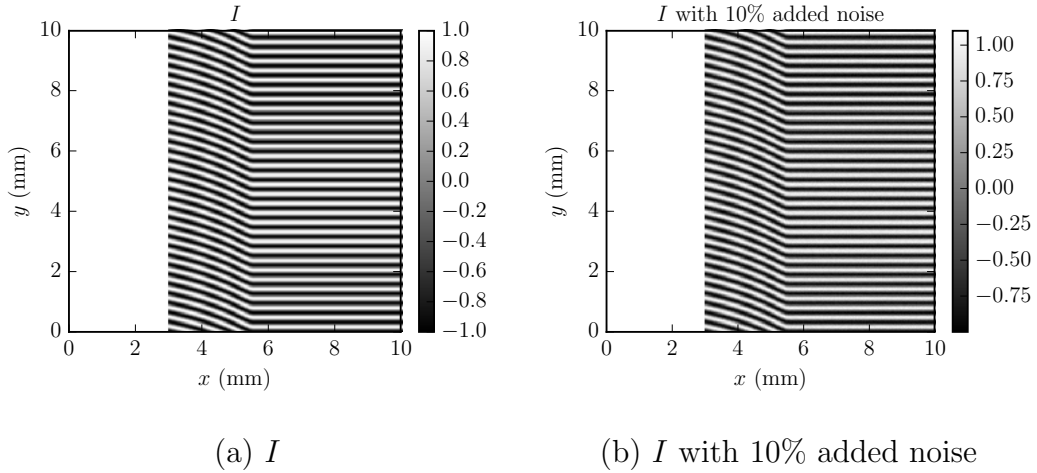


Figure A.6: Synthetic interferogram with (a) no noise and (b) 10% added noise.

The error between the synthetic and processed temperature fields is shown in Fig. A.7. Figure A.7 shows that the freestream region has the lowest error. The error quickly grows in the thermal boundary layer as  $r$  approaches the centerline. Based on Fig. A.7, an error of 2% is observed in the thermal boundary layer (equivalent to the thermal boundary layer of the sphere near the region of flow separation). At the heated surface (equivalent to the sphere surface), a higher error of 15 – 30% is observed. This high error region is confined to less than 0.1 mm from the hot surface. In the freestream, the error is less than 2%. It is seen from Fig. A.7 that the error introduced by the phase demodulation procedure, inversion algorithm, and straight path

assumption are quite small in the thermal boundary layer of a sphere.

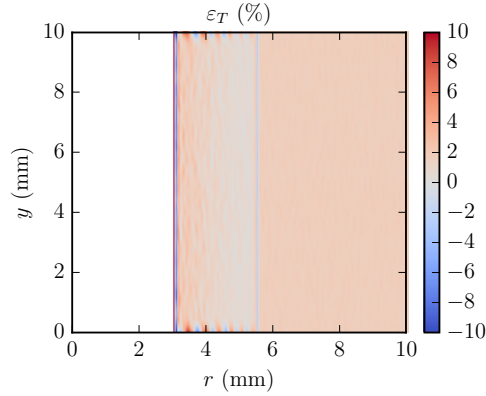


Figure A.7: Error between synthetic and processed temperature fields.

Additionally, the optical phase difference profiles calculated by using the Abel transform and the ray tracing algorithm for the temperature field of Fig. A.2 are almost identical. This indicates, that the contribution to the error from refraction is negligible. Finally, the addition of noise to the synthetic interferogram appears to alter the distribution of the error, however, it does not affect the magnitude. Therefore, the major contributions to the error come from the the phase demodulation procedure and the inversion algorithm.

- [1] C. M. Vest, *Applied Optics* 14 (1975) 1601–1606.
- [2] G. Kahl, D. C. Mylin, *Journal of the Optical Society of America* 55 (1965) 364–&.